Effect of Si-addition on structure and thermal stability of Ti-Al-N coatings

Zhe R. Liu[a], Fei Pei[a,b], Li Chen[a,b,*], Paul H. Mayrhofer[c]

[a] *State Key Laboratory of Powder Metallurgy, Central South University, Changsha 410083, China*

[b] *Zhuzhou Cemented Carbide Cutting Tools Co., Ltd., Zhuzhou 412007, China*

[c] *Institute of Materials Science and Technology, TU Wien, Vienna, Austria*

Abstract: The superior mechanical properties and thermal stability of Ti-Al-Si-N coatings have attracted extensive research interests in academia as well as industry. In this study, $Ti_{0.52}Al_{0.48}N$, $Ti_{0.53}Al_{0.38}Si_{0.09}N$, $Ti_{0.43}Al_{0.48}Si_{0.09}N$, and $Ti_{0.48}Al_{0.38}Si_{0.14}N$ coatings are developed by arc-evaporation. This compositional variation allows to study the impact of Al and Si on structure, thermal stability, and oxidation behavior. Incorporation of Si into Ti-Al-N leads to a nanocomposite structure with an amorphous-like SiN_x boundary-phase – encapsulating small crystalline Ti-Al-N grains – and promotes wurtzite-type AlN formation. This causes a significant change in the mechanical and thermal properties of the originally single-phase face-centered cubic structured $Ti_{0.52}Al_{0.48}N$. The Si-containing coatings experience an initial increase in hardness from 29.1 ± 1.0 GPa for $Ti_{0.52}Al_{0.48}N$ to 33.1 ± 1.2 GPa for $Ti_{0.53}Al_{0.38}Si_{0.09}N$, and then a decrease to 26.4 ± 0.8 GPa for $Ti_{0.43}Al_{0.48}Si_{0.09}N$ and 28.1 ± 0.8 GPa for $Ti_{0.48}Al_{0.38}Si_{0.14}N$. Alloying with Si improves the thermal stability of Ti-Al-N by retarding the decomposition towards its thermodynamically stable constituents TiN and AlN. Moreover, the oxidation resistance of Ti-Al-N can be largely improved by the Si-addition due to the retarded anatase-to-rutile TiO_2 transformation as well as the formation of a protective oxide scale at the nitride-to-oxide interface. Cross-sectional scanning electron microscopy studies reveal that the oxide scales of the Si-containing coatings exhibit a lamellar structure comprising Al-rich, TiSi-rich, and/or Ti-rich oxide layers. Higher Si and, especially, higher Al content is favorable to the formation of an Al-rich layer, which can act as a diffusion barrier for oxygen. Especially, all Si-containing coatings present an abnormal oxidation behavior, where the consumed nitride layer thickness is not continuously increasing with oxidation temperature.

Keywords: Coating; TiAlSiN; Thermal stability; Oxidation behavior

* Corresponding author. E-mail address: chenli_927@126.com (L. Chen)

1. Introduction

Hard coatings utilized as surface protection for tools and components that are employed under massive mechanical and thermal loads have aroused comprehensive research interests in recent decades [1]. Among them, face-centered cubic (simply abbreviated with c, NaCl-type, B1) Ti-Al-N coatings play a predominant role in industrial applications due to their outstanding mechanical properties, thermal stability, and especially the age-hardening ability. The latter stems from thermally triggered spinodal decomposition causing the formation of coherent Al-rich and even Ti-rich nitride domains, which hamper dislocation glide and motion [2-5]. Moreover, Ti-Al-N provides good oxidation resistance especially if a dense and protective Al_2O_3-rich layer is formed on top of the coating. With increasing Al content, the typically alternating Ti-rich and Al-rich oxide scale growth allows the formation of a dense and protective Al_2O_3-rich outermost layer. However, for Al contents below 75% (of the metal species) still a porous TiO_2-rich layer is present, which initially crystallizes with its metastable anatase structure (a-TiO_2). With increasing time and/or temperature, this metastable phase transforms towards its thermodynamically stable rutile structure (r-TiO_2). This transformation involves a volume contraction that leads to the formation of cracks and influences also the integrity of the Al_2O_3-rich top layer [6, 7]. Severe oxidation of (Ti,Al)N coatings already happens when they are exposed to oxidizing environments at 850 °C [8-10], which is below the requirements needed for some advanced applications, such as dry high-speed machining where temperatures at the rake face or cutting edge can easily exceed 1000 °C [11].

To tailor the structure and improve properties, the (Ti,Al)N coatings are alloyed either with

other transition elements (e.g., Zr [12], Ta [13], Cr [9], V [14]), reactive elements (e.g., Ru [15], La [16]), or semimetals (e.g., B [17] and Si [18]). Among them, but really special, is Si, which allows to exceptionally increase both the oxidation resistance and mechanical properties simultaneously. Si can substitute the elements in the c-(Ti,Al)N lattices up to a certain extent but is also responsible for the formation of a nanocrystalline (nc-) respectively nanocomposite structure, where nc-(Ti,Al)N grains are embedded in an amorphous-like (a-) SiN_x phase [19-22]. If the interfacial a-SiN_x phase is thin, the cohesive strength of the boundaries is increased leading to extremely high hardness of such alloyed (Ti,Al)N coatings [19, 21, 23]. Additionally, the a-SiN_x interfacial phase can retard the decomposition of nc-(Ti,Al)N grains towards their thermodynamically stable constituents TiN and AlN, thus further improving the thermal stability [24, 25]. Such nc-(Ti,Al)N/a-SiN_x nanocomposite coatings remain their high hardness up to 1100 °C, while the Si-free (Ti,Al)N coatings yield decomposition and softening already at about 800 to 900 °C [25]. Their improved oxidation resistance can be associated with the following points: The a-SiN_x interfacial phase suppresses the contact of nc-(Ti,Al)N grains with oxygen by acting as a diffusion barrier [26]. Si effectively retards the phase-transition of anatase TiO_2 to rutile TiO_2 and thereby reduces the crack-formation within the oxide scale [26-28]. Si promotes the formation of a protective outermost Al_2O_3 layer by supporting the preferential diffusion of Al to the air/oxide interface [29, 30]. Si allows to form a dense and well-adherent inner oxide layer at the nitride interface [31]. However, an unsolved question arises from one of our previous studies [24], where we showed that the oxide scale thickness of Ti-Al-Si-N coatings is thinner after oxidizing at 1000 °C than at 950 °C.

To provide further evidence and explanations for this anomalous oxidation behavior, we investigated Ti-Al-Si-N coatings having different Si and Al contents. $Ti_{0.52}Al_{0.48}N$, $Ti_{0.53}Al_{0.38}Si_{0.09}N$, $Ti_{0.43}Al_{0.48}Si_{0.09}N$, and $Ti_{0.48}Al_{0.38}Si_{0.14}N$ coatings – arc evaporated from corresponding cathodes with Si/Ti ratios of 0, 0.17, 0.21, and 0.29 and Al/(Ti+Al+Si) ratios of 0.48 and 0.38 in N_2 atmosphere – were investigated in detail after oxidation in synthetic air at 850, 900, 950 and 1000 °C for up to 15 hours. To complement the study, also hardness and phase stability changes upon exposure to vacuum annealing (up to 1200 °C) are discussed.

2. Experimental process

2.1 Coating preparation

Ti-Al-N and Ti-Al-Si-N coatings were deposited in a commercial cathodic arc evaporation system (Oerlikon Balzers, Rapid Coating System, RCS) equipped with $Ti_{0.50}Al_{0.50}$, $Ti_{0.50}Al_{0.40}Si_{0.10}$, $Ti_{0.40}Al_{0.50}Si_{0.10}$, and $Ti_{0.45}Al_{0.40}Si_{0.15}$ alloyed cathodes. The vacuum chamber was preheated to 500 °C and pumped to a base pressure less than 1.0×10^{-3} Pa before deposition. During deposition, the process was performed in a N_2 atmosphere (99.999 % purity) at a pressure of 3.2 Pa. The substrate bias and the target current were set at −40 V and 180 A, respectively. Multiple substrates including cemented carbide blocks (WC-6 wt% Co, 12 × 8 × 4 mm^3), low-alloy steel foils (200 × 100 × 0.1 mm^3), tungsten pieces and corundum sheets (10 × 10 × 1 mm^3) were chosen to meet the requirements of various measurements. All samples were cleaned in ethanol and acetone using an ultrasonic cleaning machine to strengthen the adhesion between substrates and coatings prior to deposition.

2.2 Thermal treatment

To acquire free-standing coating powders for the subsequent thermal treatment, the coated low-alloy steel foils were immersed in 10 mol.% nitric acid to remove the substrates. Annealing treatments were carried out in thermal gravimetric analysis (TGA, Netzsch-STA 409C) from room temperature (RT) to specified annealing temperature (T_a) in flowing Ar (99.9% purity, 20 sccm flow rate) or flowing synthetic air (21% O_2, 79% N_2, 20 sccm flow rate) atmosphere. The powdery samples were cooled down immediately with a cooling rate of 50 K/min after the furnace was heated to a specified temperature with a heating rate of 10 K/min. The coated tungsten pieces were isothermally annealed for 30 min from 800 to 1200 °C with a step of 100 °C in a vacuum furnace (COD533R, Germany). The annealing process was performed with a pressure below 1×10^{-4} Pa and a heating rate of 5 K/min. For the coated corundum sheets, 15-hour isothermal oxidation at 850, 900, 950, and 1000 °C was conducted by the aforementioned TGA equipment after which fracture cross-sections were prepared to be studied by scanning electron microscopy (SEM) for the oxide layers formation. For $Ti_{0.48}Al_{0.38}Si_{0.14}N$ an additional 10-hour isothermal oxidation experiment was carried out.

2.3 Sample characterization

Fractured cross-sectional morphologies of oxidized coatings were obtained using a scanning electron microscopy (SEM, Zeiss Supra 55) operated at 25 kV under backscattering mode. The cross-sections were also investigated for the chemical variation from the outermost surface down to the substrate by energy dispersive X-ray spectroscopy (EDX, Oxford Instrument X-Max) line scans. Crystalline phase structures were evaluated by X-ray diffraction

(XRD, Bruker AXS D8 Advance) with Cu Kα radiation (λ = 1.541 Å). The growth morphology of the as-deposited coatings was studied with an aberration-corrected transmission electron microscopy (TEM, FEI Titan G2 60-300 operated at 300 kV). A dual-beam focused ion beam (FIB) system (FEI Helios Nanolab 600i) was utilized to prepare the TEM specimens and final surface cleaning was conducted at 5 kV and 41 pA to minimize the damage induced by FIB. The hardness (H) and indentation modulus of the coatings were obtained according to the Oliver and Pharr method [32] using nanoindentation (Anton Paar NHT^2) equipped with a Berkovich diamond tip. In order to avoid the interference of substrates, a small load of 15 mN, which was according to our previous experience, was managed to maintain the depth of indentation less than 10% of the thickness of the coatings. At least fifteen repetitive indentations were conducted for each sample to obtain their values.

3. Results and discussion

3.1 Composition, structure and mechanical properties

Chemical compositions of our $Ti_{1-x-y}Al_xSi_yN$ coatings determined by EDX analysis are $Ti_{0.52}Al_{0.48}N$, $Ti_{0.53}Al_{0.38}Si_{0.09}N$, $Ti_{0.43}Al_{0.48}Si_{0.09}N$, and $Ti_{0.48}Al_{0.38}Si_{0.14}N$, corresponding to the targets of $Ti_{0.50}Al_{0.50}$, $Ti_{0.50}Al_{0.40}Si_{0.10}$, $Ti_{0.40}Al_{0.50}Si_{0.10}$ and $Ti_{0.45}Al_{0.40}Si_{0.15}$, respectively. Here, we want to mention that the notation $Ti_{1-x-y}Al_xSi_yN$ shall not imply that Ti, Al, and Si share the same metal sublattice. The notation basically gives the relative fraction of the elements Ti, Al, and Si. The compositional deviation between the coatings and targets stems from gas scattering, preferential resputtering of lighter Al and Si elements, and the different degrees of ionization of Ti, Al, and Si during the deposition process [33]. Fig. 1 presents the XRD patterns of as-

deposited Ti-Al-N and Ti-Al-Si-N coatings. The structure of $Ti_{0.52}Al_{0.48}N$ can be described by a well-crystallized single-phase face-centered cubic solid solution whereas all Si-containing coatings exhibit a mixed cubic-wurtzite dual-phase structure. This phase transformation is closely related to the amount of Al and Si in the coatings. Higher Al or Si contents promote the formation of the wurtzite-type (simply abbreviated with w, ZnS-wurtzite, B4) AlN-based solid solution over the cubic TiN-based solid solution [24, 28]. This phenomenon is more obvious in our Al-rich $Ti_{0.43}Al_{0.48}Si_{0.09}N$ coatings and Si-rich $Ti_{0.48}Al_{0.38}Si_{0.14}N$ coatings providing a more intense XRD signal at the positions close to w-AlN. Their broader diffraction peaks further indicate smaller coherently diffracting domain sizes, which is caused by the competitive growth of cubic and wurtzite phases. No evidence for a crystalline SiN_x phase is obtained by XRD, in agreement with earlier studies of this type of coatings [19, 34].

Further microstructural details of the Si-containing coatings are studied by cross-sectional TEM, selected area electron diffraction (SAED), and high-resolution TEM (HRTEM) of $Ti_{0.48}Al_{0.38}Si_{0.14}N$ in Fig. 2. Bright-field (BF) TEM investigations reveal a featureless structure (no columnar growth) with very small grain sizes. The corresponding SAED pattern, Fig. 2b, shows continuous diffraction rings (typical for small grains) that can be assigned to c-Ti(Al)N and w-Al(Ti)N, in excellent agreement with XRD results. HRTEM investigations (Fig. 2c) reveal nanocrystals (with sizes of about 5 nm) embedded in an amorphous-like matrix, in good agreement with the well-studied c-TiN/a-SiN_x nanocomposite structure [35, 36]. The coating with a lower Si-content but comparable Al-fraction, $Ti_{0.53}Al_{0.38}Si_{0.09}N$, exhibits a similar microstructure, which is presented in our previous study [18]. Based on our previous study on

$Ti_{1-x}Si_xN$ coatings – where we showed that Si can substitute for Ti up to $x \leq 0.17$ [35] – we envision that also for the Ti-Al-Si-N coatings a huge fraction of Si can be incorporated in the cubic phase as substitutional atom. Based on XRD and detailed TEM studies, the maximum Si fraction (as a substitutional atom in $Ti_{1-x-y}Al_xSi_yN$ with $x \sim 0.38$) is slightly below $y = 0.09$.

The hardness of $Ti_{0.52}Al_{0.48}N$ is 29.1 ± 1.0 GPa, lower than that of $Ti_{0.53}Al_{0.38}Si_{0.09}N$ (33.1 ± 1.2 GPa), Fig. 3. Typically nc-(Ti,Al)N/a-SiN_x nanocomposite coatings provide a higher hardness than (Ti,Al)N, due to grain refinement, increased cohesive strength of the grain boundaries and hindered dislocation movement by the a-SiN_x interfacial phase [22]. Additionally, solid solution hardening is also active when Si atoms are at the sublattices of c-(Ti,Al)N lattices as well. All these mechanisms help to increase the strength of c-(Ti,Al)N as long as the fraction of the typically softer w-AlN-based phase is negligible [37], like for the $Ti_{0.53}Al_{0.38}Si_{0.09}N$. Because there is a considerable amount of the typically soft w-AlN-based phase in the higher Al-containing ($Ti_{0.43}Al_{0.48}Si_{0.09}N$) or higher Si-containing ($Ti_{0.48}Al_{0.38}Si_{0.14}N$) coating, their hardness is with 26.4 ± 0.8 and 28.1 ± 0.8 GPa, respectively, below that of $Ti_{0.52}Al_{0.48}N$. Si-addition also gives rise to a decrease in elastic modulus of Ti-Al-N coatings, which can be associated with the formation of the w-AlN-based phase having lower moduli.

3.2 Thermal stability

The XRD patterns of (a) $Ti_{0.52}Al_{0.48}N$, (b) $Ti_{0.53}Al_{0.38}Si_{0.09}N$, (c) $Ti_{0.43}Al_{0.48}Si_{0.09}N$, and (d) $Ti_{0.48}Al_{0.38}Si_{0.14}N$ powdery coatings after annealing in an inert atmosphere Ar at given temperatures (T_a) are shown in Fig. 4 to describe the thermally induced structural evolution. After annealing at 800 °C, the diffraction peaks of $Ti_{0.52}Al_{0.48}N$ marginally shift towards a

higher 2θ angle compared to the as-deposited state. This indicates rearrangement of microstructural defects to lower energy sites, which thereby reduce defect density and stresses within the coatings, see Fig. 4a. The shoulder peaks present at the left side of 2θ ~36.7° and ~42.6° at T_a of 900 °C, indicates the formation of Ti-rich cubic-structured domains pointing towards a spinodal decomposition. The increased shoulder intensity and the additional formation of a right shoulder of these peaks (indicative for the formation of Al-rich cubic-structured domains) evidences the proceeding of spinodal decomposition in this $Ti_{0.52}Al_{0.48}N$ material when annealed at 1000 °C. Even higher temperatures, T_a = 1100 °C, allow for the formation of the thermodynamically stable w-AlN phase (see the additional peak 2θ ~33.2°). This progress continuously proceeds to 1300 °C and is in excellent agreement to earlier studies on this material system [38-41]. Further elevating the annealing temperature to 1450 °C results in a completed decomposition of the initially single-phase c-$Ti_{0.52}Al_{0.48}N$ into its stable constituents c-TiN and w-AlN. The $Ti_{0.53}Al_{0.38}Si_{0.09}N$ coating, when compared with $Ti_{0.52}Al_{0.48}N$, has its major XRD peaks – indicative for the c-TiN-based phase at smaller 2θ angles, Fig. 4b. And up to T_a = 1100 °C there are no big microstructural changes, according to the similar XRD patterns, which only show a slightly increasing background in the 2θ range 33–36°. For $T_a \geq 1200$ °C, peaks at the 2θ position for w-AlN develop while the major coating peaks move towards c-TiN, indicating the formation of the stable constituents c-TiN and w-AlN. After annealing at 1550 °C, the additional peak at 2θ ~28.4° points towards the formation of a crystalline Si phase. The higher Al or Si containing coatings, $Ti_{0.43}Al_{0.48}Si_{0.09}N$ and $Ti_{0.48}Al_{0.38}Si_{0.14}N$, exhibit a comparable evolution of their microstructure with annealing

temperature as indicated by their XRD patterns, Figs. 4c and d, respectively. Only that the formation of the more developed XRD peaks indicative for w-AlN formation is shifted to higher temperatures (1300 instead of 1200 °C) for the higher Si-containing coating. Additionally, after annealing at the highest temperature used (1550 °C), a crystalline alpha Si_3N_4 for higher Si-containing coating can be detected, in addition to the Si phase (see Fig. 4d).

The microstructural changes of the Ti-Al-N and Si-alloyed Ti-Al-N coatings induce also hardness changes, see Fig. 5. The hardness of $Ti_{0.52}Al_{0.48}N$ peaks at T_a = 800 °C with 33.5 ± 0.8 GPa, that of $Ti_{0.53}Al_{0.38}Si_{0.09}N$ at T_a = 1000 °C with 36.7 ± 0.7 GPa, that of $Ti_{0.43}Al_{0.48}Si_{0.09}N$ at T_a = 1000 °C with 28.1 ± 1.0 GPa, and that of $Ti_{0.48}Al_{0.38}Si_{0.14}N$ at T_a = 1000 °C with 29.7 ± 0.9 GPa. As soon as a considerable fraction of w-AlN is formed, the hardness decreases. Due to the different annealing procedure (the samples used for hardness measurements are isothermally annealed for 30 min after reaching T_a with 5 K/min, whereas those for detailed XRD investigations are immediately cooled down after reaching T_a with a heating rate of 10 K/min), the hardness reduction due to the formation of w-AlN is obtained at ~100 °C lower temperatures than suggested by the detailed XRD investigations, Fig. 4. This has been verified by XRD investigations of samples used for the hardness measurements (see supplementary data). Clearly, all Si-containing coatings outperform the $Ti_{0.52}Al_{0.48}N$ for $T_a \geq 1000$ °C.

3.3 Oxidation resistance

Detailed XRD investigations of $Ti_{0.52}Al_{0.48}N$, $Ti_{0.53}Al_{0.38}Si_{0.09}N$, $Ti_{0.43}Al_{0.48}Si_{0.09}N$, and $Ti_{0.48}Al_{0.38}Si_{0.14}N$ (removed from their low-alloy steel substrates) after annealing in synthetic air at 850 to 1200 °C are presented in Figs. 6a, b, c, and d, respectively (except for the

atmosphere, the annealing procedure is identical to that used for the vacuum annealing treatment presented in Fig. 4). The oxidation products of $Ti_{0.52}Al_{0.48}N$ at T_{ox} = 850 °C are dominated by anatase-structured (a-) TiO_2 next to rutile (r-) TiO_2, see Fig. 6a. No crystalline α-Al_2O_3 can be detected. After oxidizing at T_{ox} = 950 °C, the peak intensities of a-TiO_2 and r-TiO_2 increase and their ratio (r-TiO_2/a-TiO_2) increases as well. A tiny diffraction peak at ~35.2° indicates the formation of corundum type α-Al_2O_3. Increasing T_{ox} to 1000 °C further promotes the formation of crystalline α-Al_2O_3 as well as the anatase-to-rutile TiO_2 transformation leading to decreased a-TiO_2 and increased r-TiO_2 signals. After oxidation at T_{ox} = 1100 and 1200 °C, no remaining nitride phases can be detected anymore and also no a-TiO_2; the XRD patterns basically consist of α-Al_2O_3 and r-TiO_2 contributions. Oxidizing $Ti_{0.53}Al_{0.38}Si_{0.09}N$ at 850 °C only leads to the formation of a rather weak XRD peak at ~25.3°, indicative for a-TiO_2, Fig. 6b. Oxidation at T_{ox} = 950 °C, also lead here (corresponding to the Si-free sample, $Ti_{0.52}Al_{0.48}N$) to the formation of corundum type α-Al_2O_3 and r-TiO_2. But contrary to $Ti_{0.52}Al_{0.48}N$, still some nitride phases and a-TiO_2 can be detected after oxidation at T_{ox} = 1100 °C. Even after oxidation at 1200 °C, still a-TiO_2 is present, suggesting that the Si-addition retards the anatase-to-rutile transformation. The higher Al or Si containing coatings, $Ti_{0.43}Al_{0.48}Si_{0.09}N$ and $Ti_{0.48}Al_{0.38}Si_{0.14}N$, exhibit no sign of crystalline oxide products after oxidizing at 850 °C, see Figs. 6c and d, respectively. Increasing T_{ox} up to 950 °C, clearly a-TiO_2, r-TiO_2, and α-Al_2O_3 can be detected for both samples. Their intensity and the anatase-to-rutile ratio increase with increasing T_{ox}. After oxidation at 1100 °C, still some nitride phases can be detected with lower intensity for the higher Si-containing coating, $Ti_{0.48}Al_{0.38}Si_{0.14}N$, Fig. 6d. For both coatings a

considerable contribution still comes from a-TiO_2, indicating that the higher Al or Si content helps to hinder the anatase-to-rutile transformation (considering that the $Ti_{0.53}Al_{0.38}Si_{0.09}N$ sample with lower Al and Si content exhibits weaker a-TiO_2 signals at the same T_{ox}). The small diffraction signals marked with black arrows in Figs. 6c and d stem from an Al_2TiO_5 phase formation.

Overall, the detailed XRD investigations after oxidation at various temperatures showed that Si-addition not just retards the formation of crystalline TiO_2 but also its transformation from the initially formed anatase-phase towards the thermodynamically stable rutile-phase.

To study the oxide scale morphology especially of the Si-containing coatings, as those for $Ti_{0.52}Al_{0.48}N$ have already been presented in Ref. [18], $Ti_{0.53}Al_{0.38}Si_{0.09}N$, $Ti_{0.43}Al_{0.48}Si_{0.09}N$, and $Ti_{0.48}Al_{0.38}Si_{0.14}N$ (on sapphire substrates) are isothermally oxidized in synthetic air for 15 h. Fig. 7 shows the cross-sectional SEM and line scan images of $Ti_{0.53}Al_{0.38}Si_{0.09}N$ after 15-hour isothermal oxidation at 850 °C (a and d), 900 °C (b and e), and 950 °C (c and f). Whereas the line scans indicate that all oxide scales are composed of a Ti-rich top layer, an Al-rich interlayer, and a (Ti,Si)-rich sublayer (Figs. 7d, e, and f); their growth morphology is dense and homogenous. The compositional variation along the oxide scale thickness is comparable to that of $Ti_{0.52}Al_{0.48}N$ [9, 10]. The oxide scales of $Ti_{0.43}Al_{0.48}Si_{0.09}N$ grown at 850, 900, and 950 °C are all much thinner than those of the lower Al-containing $Ti_{0.53}Al_{0.38}Si_{0.09}N$ at the corresponding temperature, Fig. 8. Also, the higher Si-containing coating provides a better oxidation resistance, which is, however, not as improved (compared with $Ti_{0.53}Al_{0.38}Si_{0.09}N$) as when increasing the Al content (see Fig. 9). The compositional variation along the oxide scale thickness is similar

for $Ti_{0.48}Al_{0.38}Si_{0.14}N$ and $Ti_{0.43}Al_{0.48}Si_{0.09}N$ with an Al-rich top layer and a (Ti,Si)-rich sublayer after oxidation at 850 °C (Fig. 9a). Contrary, oxidation at higher temperatures, 900 and 950 °C, led to the formation of oxide scales that are comparable between $Ti_{0.48}Al_{0.38}Si_{0.14}N$ and the lower Al-containing $Ti_{0.53}Al_{0.38}Si_{0.09}N$ coating. There, a Ti-rich top layer, an Al-rich interlayer, and a (Ti, Si)-rich sublayer is present, Figs. 9b and c. This compositional separation in the oxide scale is related to the selective oxidation of Al due to the more negative formation energy of aluminum oxide and the weaker bonding of aluminum nitride [42]. The outward diffusion of Al (being faster than Ti and Si) towards the air/oxide interface and the inward diffusion of oxygen towards the oxide/nitride interface cause the formation of an Al-rich oxide top layer and a (Ti,Si)-rich oxide sublayer [42, 43]. A dense Al-rich oxide top layer (mainly consisting of α-Al_2O_3) is favored for excellent oxidation protection of Ti-Al-N-based coatings, as it provides the best barrier to ion transport [44]. With proceeding oxidation, the anatase-structured TiO_2 gradually transforms towards the thermodynamically stable rutile-structured TiO_2, which involves an overall volume contraction and thereby triggers the initiation of cracks [6, 10, 44]. These will expand throughout the Al-rich oxide by which fast diffusion pathways for oxygen are provided. We maintain that now the Si-rich regions help to “seal” the entire interface to the remaining nitride by forming the inner (Ti,Si)-rich oxide layer [31].

The results clearly indicate that an optimized combination of Al and Si is important to obtain best oxidation resistance. The thinnest oxide scale, with an intact bilayer-structure up to 950 °C, is provided by $Ti_{0.43}Al_{0.48}Si_{0.09}N$, which combines a high Al content with a moderate Si content. This allows the formation of a dense protective Al-rich outer oxide layer and a (Ti,Si)-

rich inner oxide layer. The higher Si- but lower Al-containing coating, $Ti_{0.48}Al_{0.38}Si_{0.14}N$, also exhibits excellent oxidation resistance as even after 15-hour isothermal oxidation at 1000 °C the (originally ~3-μm-thin) coating is not fully oxidized (not shown here). Contrary, the coating with the same Si- but lower Al-content, $Ti_{0.53}Al_{0.38}Si_{0.09}N$, (with respect to the best coating, $Ti_{0.43}Al_{0.48}Si_{0.09}N$) is fully oxidized after a 15-hour isothermal oxidation at 1000 °C. But also this one provides a much better oxidation protection than the Si-free coating, $Ti_{0.52}Al_{0.48}N$, which (regardless of its higher Al-content) already completely oxidized when exposed for 10 h to air at 850 °C [45]. Our XRD results presented in Fig. 6 demonstrate that the oxidation resistance of $Ti_{0.52}Al_{0.48}N$ is positively influenced by Si-addition due to the prevented crystalline TiO_2 formation and also the retarded anatase-to-rutile transformation. Additionally, the inner (Ti,Si)-rich oxide layer, which is supposed to be an admixed TiO_2-SiO_2 oxide [46], can also protect the remaining nitride because the SiO_2 is viscous (especially at higher temperatures) allowing to "seal" cracks and pores [31].

Interestingly, the oxide scale on $Ti_{0.53}Al_{0.38}Si_{0.09}N$ is thinner for the higher oxidation temperature of 900 °C (1.12 ± 0.10 μm) than for 850 °C (1.21 ± 0.07 μm), see Figs. 7a and b. The comparison of the remaining nitride (which is also thicker for the higher T_{ox} of 900 °C) shows that this behavior is not to explain with the formation of volatile oxidation products. Clearly, the oxide-scale has a better protective behavior when grown at the higher oxidation temperate of 900 °C. The higher Si- but same Al-containing coating, $Ti_{0.48}Al_{0.38}Si_{0.14}N$, shows a comparable behavior when increasing the oxidation temperature from 900 to 950 °C, after which the oxide scale is 1.87 ± 0.15 μm and 1.62 ± 0.11 μm thin, respectively (see Figs.

9b and c). Such a phenomena is not observed for Si-free Ti-Al-N [47] and not that obvious for the higher Al- but same Si-containing coating, $Ti_{0.43}Al_{0.48}Si_{0.09}N$ (with respect to $Ti_{0.53}Al_{0.38}Si_{0.09}N$, where this phenomena is most pronounced), which showed the thinnest oxide scales among all coatings investigated for 800, 900, and 950 °C, see Fig. 8. But when investigating the remaining nitride layer thickness, also this coating shows a somehow anomalous behavior, with a thicker remaining nitride for T_{ox} = 900 than for T_{ox} = 850 °C, compare Figs. 8b and a, respectively.

Considering this important outcome, looking at the consumed nitride layer thickness in more detail is necessary, Fig. 10. All three Si-containing coatings show that the consumed nitride layer thickness is not continuously increasing with oxidation temperature. The lower Si containing coatings, $Ti_{0.53}Al_{0.38}Si_{0.09}N$ and $Ti_{0.43}Al_{0.48}Si_{0.09}N$, show a minimum at T_{ox} = 900 °C, whereas the higher Si-containing one, $Ti_{0.48}Al_{0.38}Si_{0.14}N$, shows that the nitride layer is less consumed during oxidation at 950 °C than at 900 °C. As mentioned above, such a behavior has never been observed for Si-free Ti-Al-N, clearly connecting this phenomenon to the addition of Si. We envision that the Si-effect is multifold. Si is able to form a protective oxide scale at the nitride-to-oxide interface, as nicely shown for Si-doped high entropy nitrides [31], and Si retards the anatase-to-rutile transformation. While for Si-free Ti-Al-N there is no a-TiO_2 detectable anymore for $T_{ox} \geqslant$ 1100 °C, the Si-containing coatings exhibit a-TiO_2 even after oxidation at 1200 °C, see Fig. 6. Based on these XRD results a Si/Ti ratio of 0.21 ($Ti_{0.43}Al_{0.48}Si_{0.09}N$) seems to be most effective in retarding the a-TiO_2-to-r-TiO_2 transformation. The coatings with higher Si/Ti-ratio (0.29 for $Ti_{0.48}Al_{0.38}Si_{0.14}N$) or lower ratio (0.17 for $Ti_{0.53}Al_{0.38}Si_{0.09}N$) exhibit a higher rutile-to-anatase intensity ratio for T_{ox} = 1100 and 1200 °C. Up

to 1000 °C, the intensity ratio between r-TiO_2 (110, at 27.4°) and a-TiO_2 (101, at 25.3°) is still below 1 for the Si-containing films, therefore these films (and especially $Ti_{0.43}Al_{0.48}Si_{0.09}N$, which exhibits an intensity ratio of 0.39) will experience a less-pronounced a-TiO_2-to-r-TiO_2 connected transformation-induced volume contraction. Hence, for these oxide scales there is a reduced initiation of cracks at these elevated temperatures, which promotes the formation of a dense and protective outer α-Al_2O_3-based oxide scale. For the Ti-Al-Si-N coatings with a higher or lower Si/Ti ratio than 0.21 ($Ti_{0.53}Al_{0.38}Si_{0.09}N$ and $Ti_{0.48}Al_{0.38}Si_{0.14}N$) the outermost oxide scale is already Ti-rich after the 15-h isothermal oxidation at 900 and 950 °C, Figs. 7 and 9. This is not the case for $Ti_{0.43}Al_{0.48}Si_{0.09}N$ (with a Si/Ti-ratio of 0.21), which shows the Al-rich oxide scale as the top layer even after oxidation at 950 °C. Based on these results we envision that the a-TiO_2-to-r-TiO_2 transformation cracks the outermost Al_2O_3-based oxide scale. Thereby, fast-diffusion pathways for Ti are provided, which then forms the outermost Ti-rich oxide.

To further prove this scenario, the $Ti_{0.48}Al_{0.38}Si_{0.14}N$ coating (Si/Ti ratio of 0.29) was investigated after a shorter exposure (10 h) to the isothermal oxidation treatment at 850, 900, and 950 °C. The corresponding cross-sectional SEM investigations, Figs. 11a, b, and c, respectively, again show that the oxide scale is thinner with a thicker remaining nitride layer when oxidation is conducted at 950 °C instead of 900 °C (0.87 ± 0.01, 1.75 ± 0.07, and 1.39 ± 0.07 μm oxide scale thickness for T_{ox} = 850, 900, and 950 °C, respectively). Now the EDS line scans prove that the outermost oxide layer is Al-rich. Noticeably, as shown by the local enlarged insets of Figs. 11c and b, the Al-rich oxide layer is denser when grown at 950 °C than at 900 °C, respectively. The line scan signal for Ti slightly increases at the outermost region

of the oxide scale grown at 850, 900 and 950 °C, see Figs. 11d, e, and f, respectively, suggesting that Ti atoms are about to diffuse towards the air/oxide interface. This is increasingly pronounced for increasing oxidation temperature. Therefore, after 15 h the outermost oxide scale is clearly Ti-rich with T_{ox} = 900 and 950 °C.

4. Conclusions

The effect of Si-addition on structure and thermal stability of arc-evaporated (Ti,Al)N coatings is investigated. $Ti_{0.52}Al_{0.48}N$ exhibits a well-crystallized single-phase face-centered cubic structure, whereas Si-containing $Ti_{0.53}Al_{0.38}Si_{0.09}N$, $Ti_{0.43}Al_{0.48}Si_{0.09}N$, and $Ti_{0.48}Al_{0.38}Si_{0.14}N$ have a nanocomposite structure of nanometer-sized cubic and wurtzite crystalline grains fully encapsulated by an amorphous-like SiN_x boundary-phase. This structural evolution – from a single-phase c-(Ti,Al)N to a nc-(Ti,Al)N/a-SiN_x – results in an improved hardness (from 29.1 ± 1.0 GPa for $Ti_{0.52}Al_{0.48}N$ to 33.1 ± 1.2 GPa for $Ti_{0.53}Al_{0.38}Si_{0.09}N$) as long as the formation of the softer wurtzite-type phase is minor. The latter is promoted by the alloying with Si, and therefore the $Ti_{0.43}Al_{0.48}Si_{0.09}N$ (higher Al than $Ti_{0.53}Al_{0.38}Si_{0.09}N$) and $Ti_{0.48}Al_{0.38}Si_{0.14}N$ (higher Si than $Ti_{0.53}Al_{0.38}Si_{0.09}N$) again exhibit a lower hardness of 26.4 ± 0.8 and 28.1 ± 0.8 GPa, respectively. Furthermore, the incorporation of Si effectively retards the decomposition of the supersaturated (Ti,Al)N solid solution towards its thermodynamically stable constituents c-TiN and w-AlN. This prolongs the age-hardening effect of this type of material from 800 to 1000 °C and leads to a better performance in mechanical properties especially for annealing temperatures (or application temperatures) above 1000 °C.

Probably even more important is the enormous impact that Si applies to the oxidation resistance of Ti-Al-N coatings. The results presented here clearly prove that the Si-effect is multifold: The a-SiN_x interfacial phase acts as a diffusion barrier, and if TiO_2 is formed, Si retards its phase-transition from anatase to rutile. This reduces the thereby connected crack-formation within the oxide scale. Furthermore, Si promotes the formation of a protective outermost Al_2O_3 layer (at the interface to the ambient air) and a dense, well-adherent inner oxide layer (at the interface to the underlying nitride layer). The anatase-to-rutile transformation largely depends on the Si/Ti ratio of the Ti-Al-Si-N coatings. The Si/Ti ratio of 0.21 for $Ti_{0.43}Al_{0.48}Si_{0.09}N$ is more effective than 0.29 for $Ti_{0.48}Al_{0.38}Si_{0.14}N$ and 0.17 for $Ti_{0.53}Al_{0.38}Si_{0.09}N$ to retard this transformation, and therefore the $Ti_{0.43}Al_{0.48}Si_{0.09}N$ will experience fewer crack formation. This helps to keep the protective oxide scale intact and the oxidation resistance high. All three Si-containing coatings present an abnormal oxidation behavior, where the consumed nitride layer thickness is not continuously increasing with oxidation temperature. This is because a denser and more protective Al-rich layer is formed at a higher oxidation temperature, which is supported by the Si-alloying.

Acknowledgments

We gratefully acknowledge financial support by the National Natural Science Foundation of China under Grant No. 51775560 and the State Key Laboratory of Powder Metallurgy from Central South University of China.

References

[1] A.A. Voevodin, C. Muratore, S.M. Aouadi, Hard coatings with high temperature adaptive lubrication and contact thermal management: review, Surf. Coat. Technol. 257 (2014) 247-265. https://doi.org/10.1016/j.surfcoat.2014.04.046

[2] S. Paldey, S. Deevi, Single layer and multilayer wear resistant coatings of (Ti,Al)N: a review, Mater. Sci. Eng. A Struct. 342 (2002) 58-79. https://doi.org/10.1016/S0921-5093(02)00259-9

[3] L. Chen, Y. Du, P.H. Mayrhofer, S.Q. Wang, J. Li, The influence of age-hardening on turning and milling performance of Ti–Al–N coated inserts, Surf. Coat. Technol. 202 (2008) 5158-5161. https://doi.org/10.1016/j.surfcoat.2008.05.036

[4] A. Hörling, L. Hultman, M. Odén, J. Sjölén, L. Karlsson, Mechanical properties and machining performance of $Ti_{1-x}Al_xN$-coated cutting tools, Surf. Coat. Technol. 191 (2005) 384-392. https://doi.org/10.1016/j.surfcoat.2004.04.056

[5] J. Zhou, J. Zhong, L. Chen, L. Zhang, Y. Du, Z.-K. Liu, P.H. Mayrhofer, Phase equilibria, thermodynamics and microstructure simulation of metastable spinodal decomposition in c–$Ti_{1-x}Al_xN$ coatings, Calphad 56 (2017) 92-101. https://doi.org/10.1016/j.calphad.2016.12.006

[6] R. Hollerweger, H. Riedl, M. Arndt, S. Kolozsvari, S. Primig, P.H. Mayrhofer, Guidelines for increasing the oxidation resistance of Ti-Al-N based coatings, Thin Solid Films 688 (2019) 137290. https://doi.org/10.1016/j.tsf.2019.05.009

[7] D.A.H. Hanaor, C.C. Sorrell, Review of the anatase to rutile phase transformation, Journal of Materials Science 46 (2011) 855-874. https://doi.org/10.1007/s10853-010-5113-0

[8] D. McIntyre, J.E. Greene, G. Håkansson, J.E. Sundgren, W.D. Münz, Oxidation of metastable single‐phase polycrystalline $Ti_{0.5}Al_{0.5}N$ films: Kinetics and mechanisms, J. Appl. Phys. 67 (1990) 1542-1553. https://doi.org/10.1063/1.345664

[9] Y.X. Xu, L. Chen, B. Yang, Y.B. Peng, Y. Du, J.C. Feng, F. Pei, Effect of CrN addition on the structure, mechanical and thermal properties of Ti-Al-N coating, Surf. Coat. Technol. 235 (2013) 506-512. http://doi.org/10.1016/j.surfcoat.2013.08.010

[10] F. Vaz, L. Rebouta, M. Andritschky, M.F.d. Silva, J.C. Soares, Thermal oxidation of $Ti_{1-x}Al_xN$ coatings in air, J. Eur. Ceram. Soc. 17 (1997) 1971-1977. https://doi.org/10.1016/S0955-2219(97)00050-2

[11] T. Obikawa, T. Matsumura, T. Shirakashi, E. Usui, Wear characteristic of alumina coated and alumina ceramic tools, J. Mater. Process. Technol. 63 (1997) 211-216. https://doi.org/10.1016/S0924-0136(96)02626-X

[12] S.A. Glatz, R. Hollerweger, P. Polcik, R. Rachbauer, J. Paulitsch, P.H. Mayrhofer, Thermal stability and mechanical properties of arc evaporated Ti–Al–Zr–N hard coatings, Surf. Coat. Technol. 266 (2015) 1-9. https://doi.org/10.1016/j.surfcoat.2015.01.042

[13] R. Aninat, N. Valle, J.B. Chemin, D. Duday, C. Michotte, M. Penoy, L. Bourgeois, P. Choquet, Addition of Ta and Y in a hard Ti-Al-N PVD coating: Individual and conjugated effect on the oxidation and wear properties, Corros. Sci. 156 (2019) 171-180. https://doi.org/10.1016/j.corsci.2019.04.042

[14] Y.X. Xu, L. Chen, F. Pei, J.L. Yue, Y. Du, Thermal stability and oxidation resistance of V-

alloyed TiAlN coatings, Ceram. Int. 44 (2018) 1705-1710. https://doi.org/10.1016/j.ceramint.2017.10.100
[15] Z.R. Liu, L. Chen, Y. Du, S. Zhang, Influence of Ru-addition on thermal decomposition and oxidation resistance of TiAlN coatings, Surf. Coat. Technol. 401 (2020). https://doi.org/10.1016/j.surfcoat.2020.126234
[16] H. Du, J. Xiong, H. Zhao, Y. Wu, W. Wan, L. Wang, Structure and properties of TiAlLaN films deposited at various bias voltages, Appl. Surf. Sci. 292 (2014) 688-694. https://doi.org/10.1016/j.apsusc.2013.12.035
[17] V. Moraes, H. Bolvardi, S. Kolozsvári, H. Riedl, P.H. Mayrhofer, Thermal stability and mechanical properties of Ti-Al-B-N thin films, Int. J. Refract. Met. Hard Mater. 71 (2018) 320-324. https://doi.org/10.1016/j.ijrmhm.2017.11.027
[18] F. Pei, H.J. Liu, L. Chen, Y.X. Xu, Y. Du, Improved properties of TiAlN coating by combined Si-addition and multilayer architecture, J. Alloys Compd. 790 (2019) 909-916. https://doi.org/10.1016/j.jallcom.2019.03.248
[19] S. Carvalho, L. Rebouta, A. Cavaleiro, L.A. Rocha, J. Gomes, E. Alves, Microstructure and mechanical properties of nanocomposite (Ti,Si,Al)N coatings, Thin Solid Films 398-399 (2001) 391-396. https://doi.org/10.1016/S0040-6090(01)01348-7
[20] A. Miletić, P. Panjan, B. Škorić, M. Čekada, G. Dražič, J. Kovač, Microstructure and mechanical properties of nanostructured Ti–Al–Si–N coatings deposited by magnetron sputtering, Surf. Coat. Technol. 241 (2014) 105-111. https://doi.org/10.1016/j.surfcoat.2013.10.050
[21] S. Veprek, M. Jilek, Super- and ultrahard nanacomposite coatings： generic concept for their preparation, properties and industrial applications, Vacuum 67 (2002) 443-449. https://doi.org/10.1016/S0042-207X(02)00229-4
[22] S. Veprek, R.F. Zhang, M.G.J. Veprek-Heijman, S.H. Sheng, A.S. Argon, Superhard nanocomposites: Origin of hardness enhancement, properties and applications, Surf. Coat. Technol. 204 (2010) 1898-1906. https://doi.org/10.1016/j.surfcoat.2009.09.033
[23] S. Veprek, Veprek-Heijman, M.J. G., Industrial applications of superhard nanocomposite coatings, Surf. Coat. Technol. 202 (2008) 5063-5073. https://doi.org/10.1016/j.surfcoat.2008.05.038
[24] L. Chen, B. Yang, Y. Xu, F. Pei, L. Zhou, Y. Du, Improved thermal stability and oxidation resistance of Al–Ti–N coating by Si addition, Thin Solid Films 556 (2014) 369-375. https://doi.org/10.1016/j.tsf.2014.01.072
[25] S. Veprek, H.D. Männling, M. Jilek, P. Holubar, Avoiding the high-temperature decomposition and softening of $(Al_{1-x}Ti_x)N$ coatings by the formation of stable superhard nc-$(Al_{1-x}Ti_x)N$/a-Si_3N_4 nanocomposite, Materials Science and Engineering: A 366 (2004) 202-205. https://doi.org/10.1016/j.msea.2003.08.052
[26] P. Steyer, D. Pilloud, J.F. Pierson, J.P. Millet, M. Charnay, B. Stauder, P. Jacquot, Oxidation resistance improvement of arc-evaporated TiN hard coatings by silicon addition, Surf. Coat. Technol. 201 (2006) 4158-4162. https://doi.org/10.1016/j.surfcoat.2006.08.023
[27] D. Pilloud, J.F. Pierson, M.C. Marco de Lucas, A. Cavaleiro, Study of the structural changes induced by air oxidation in Ti–Si–N hard coatings, Surf. Coat. Technol. 202 (2008) 2413-2417. https://doi.org/10.1016/j.surfcoat.2007.09.017

[28] M. Pfeiler, J. Zechner, M. Penoy, C. Michotte, C. Mitterer, M. Kathrein, Improved oxidation resistance of TiAlN coatings by doping with Si or B, Surf. Coat. Technol. 203 (2009) 3104-3110. https://doi.org/10.1016/j.surfcoat.2009.03.036
[29] L. Zhu, M. Hu, W. Ni, Y. Liu, High temperature oxidation behavior of $Ti_{0.5}Al_{0.5}N$ coating and $Ti_{0.5}Al_{0.4}Si_{0.1}N$ coating, Vacuum 86 (2012) 1795-1799. https://doi.org/10.1016/j.vacuum.2012.04.013
[30] Y.-Y. Chang, S.-M. Yang, High temperature oxidation behavior of multicomponent TiAlSiN coatings, Thin Solid Films 518 (2010) S34-S37. https://doi.org/10.1016/j.tsf.2010.03.020
[31] A. Kretschmer, A. Kirnbauer, V. Moraes, D. Primetzhofer, K. Yalamanchili, H. Rudigier, P.H. Mayrhofer, Improving phase stability, hardness, and oxidation resistance of reactively magnetron sputtered (Al,Cr,Nb,Ta,Ti)N thin films by Si-alloying, Surf. Coat. Technol. 416 (2021). https://doi.org/10.1016/j.surfcoat.2021.127162
[32] O. W.C., P. G.M., An improved technique for determining hardness and elastic modulus using load and displacement-sensing indentation experiments, J. Mater. Res. 7 (1992) 1564-1583. https://doi.org/10.1557/JMR.1992.1564
[33] A.O. Eriksson, J.Q. Zhu, N. Ghafoor, M.P. Johansson, J. Sjölen, J. Jensen, M. Odén, L. Hultman, J. Rosén, Layer formation by resputtering in Ti–Si–C hard coatings during large scale cathodic arc deposition, Surf. Coat. Technol. 205 (2011) 3923-3930. https://doi.org/10.1016/j.surfcoat.2011.02.007
[34] A. Flink, J.M. Andersson, B. Alling, R. Daniel, J. Sjölén, L. Karlsson, L. Hultman, Structure and thermal stability of arc evaporated $(Ti_{0.33}Al_{0.67})_{1-x}Si_xN$ thin films, Thin Solid Films 517 (2008) 714-721. https://doi.org/10.1016/j.tsf.2008.08.126
[35] F. Pei, Y.X. Xu, L. Chen, Y. Du, H.K. Zou, Structure, mechanical properties and thermal stability of $Ti_{1-x}Si_xN$ coatings, Ceram. Int. 44 (2018) 15503-15508. https://doi.org/10.1016/j.ceramint.2018.05.210
[36] S.H. Kim, J.W. Jang, S.S. Kang, K.H. Kim, Synthesis and mechanical evaluation of nanocomposite coating layer of nc-TiN/a-Si_3N_4 on SKD 11 steel by sputtering, J. Mater. Process. Technol. 130-131 (2002) 283-288. https://doi.org/10.1016/S0924-0136(02)00759-8
[37] C. Wüstefeld, D. Rafaja, V. Klemm, C. Michotte, M. Kathrein, Effect of the aluminium content and the bias voltage on the microstructure formation in $Ti_{1-x}Al_xN$ protective coatings grown by cathodic arc evaporation, Surf. Coat. Technol. 205 (2010) 1345-1349. https://doi.org/10.1016/j.surfcoat.2010.07.057
[38] M. Moser, D. Kiener, C. Scheu, P.H. Mayrhofer, Influence of Yttrium on the Thermal Stability of Ti-Al-N Thin Films, Materials 3 (2010) 1573-1592. https://doi.org/10.3390/ma3031573
[39] P.H. Mayrhofer, D. Music, J.M. Schneider, Influence of the Al distribution on the structure, elastic properties, and phase stability of supersaturated $Ti_{1-x}Al_xN$, J. Appl. Phys. 100 (2006). https://doi.org/10.1063/1.2360778
[40] P.H. Mayrhofer, A. Hörling, L. Karlsson, J. Sjölén, T. Larsson, C. Mitterer, L. Hultman, Self-organized nanostructures in the Ti–Al–N system, Appl. Phys. Lett. 83 (2003) 2049-2051. https://doi.org/10.1063/1.1608464

[41] P.H. Mayrhofer, L. Hultman, J.M. Schneider, P. Staron, H.J.I.J.o.M.R. Clemens, Spinodal decomposition of cubic $Ti_{1-x}Al_xN$: Comparison between experiments and modeling, 98 (2007) 1054-1059. https://doi.org/10.3139/146.101570
[42] S. Hofmann, H.A. Jehn, Selective oxidation and chemical state of Al and Ti in (Ti,Al)N coatings, Surf. Interface Anal. 12 (1988) 329-333. https://doi.org/10.1002/sia.740120602
[43] Y.X. Xu, L. Chen, F. Pei, Y. Du, Y. Liu, J.L. Yue, Influence of Hf on the structure, thermal stability and oxidation resistance of Ti-Al-N coatings, Thin Solid Films 565 (2014) 25-31. https://doi.org/10.1016/j.tsf.2014.06.043
[44] L. Chen, J. Paulitsch, Y. Du, P.H. Mayrhofer, Thermal stability and oxidation resistance of Ti–Al–N coatings, Surf. Coat. Technol. 206 (2012) 2954-2960. https://doi.org/10.1016/j.surfcoat.2011.12.028
[45] Y.X. Xu, L. Chen, F. Pei, Y. Du, Structure and thermal properties of TiAlN/CrN multilayered coatings with various modulation ratios, Surf. Coat. Technol. 304 (2016) 512-518. https://doi.org/10.1016/j.surfcoat.2016.07.055
[46] G. Greczynski, B. Bakhit, L. Hultman, M. Odén, High Si content TiSiN films with superior oxidation resistance, Surf. Coat. Technol. 398 (2020). https://doi.org/10.1016/j.surfcoat.2020.126087
[47] B. Yang, L. Chen, K.K. Chang, W. Pan, Y.B. Peng, Y. Du, Y. Liu, Thermal and thermo-mechanical properties of Ti–Al–N and Cr–Al–N coatings, Int. J. Refract. Met. Hard Mater. 35 (2012) 235-240. https://doi.org/10.1016/j.ijrmhm.2012.06.007

Figure captions

Fig. 1 XRD patterns of $Ti_{0.52}Al_{0.48}N$, $Ti_{0.53}Al_{0.38}Si_{0.09}N$, $Ti_{0.43}Al_{0.48}Si_{0.09}N$, and $Ti_{0.48}Al_{0.38}Si_{0.14}N$ powdery coatings in the as-deposited state.

Fig. 2 Cross-sectional TEM image (a), SAED pattern (b), and HRTEM image (c) of $Ti_{0.48}Al_{0.38}Si_{0.14}N$.

Fig. 3 Indentation hardness (H) and elastic modulus of $Ti_{0.52}Al_{0.48}N$, $Ti_{0.53}Al_{0.38}Si_{0.09}N$, $Ti_{0.43}Al_{0.48}Si_{0.09}N$, and $Ti_{0.48}Al_{0.38}Si_{0.14}N$ coatings deposited on cemented carbides.

Fig. 4 XRD patterns of (a) $Ti_{0.52}Al_{0.48}N$, (b) $Ti_{0.53}Al_{0.38}Si_{0.09}N$, (c) $Ti_{0.43}Al_{0.48}Si_{0.09}N$, and (d) $Ti_{0.48}Al_{0.38}Si_{0.14}N$ powdery coatings after annealing in Ar at given temperatures.

Fig. 5 Indentation hardness of $Ti_{0.52}Al_{0.48}N$, $Ti_{0.53}Al_{0.38}Si_{0.09}N$, $Ti_{0.43}Al_{0.48}Si_{0.09}N$, and $Ti_{0.48}Al_{0.38}Si_{0.14}N$ coatings deposited on tungsten pieces after vacuum-annealing at given temperatures.

Fig. 6 XRD patterns of (a) $Ti_{0.52}Al_{0.48}N$, (b) $Ti_{0.53}Al_{0.38}Si_{0.09}N$, (c) $Ti_{0.43}Al_{0.48}Si_{0.09}N$, and (d) $Ti_{0.48}Al_{0.38}Si_{0.14}N$ powdery coatings after oxidation at given temperatures.

Fig. 7 Cross-sectional SEM images (a, b, and c) and corresponding elemental maps (d, e,

and f) of $Ti_{0.53}Al_{0.38}Si_{0.09}N$ deposited on corundum sheets after 15-hour isothermal oxidation at 850 °C (a and d), 900 °C (b and e), and 950 °C (c and f).

Fig. 8 Cross-sectional SEM images (a, b, and c) and corresponding elemental maps (d, e, and f) of $Ti_{0.43}Al_{0.48}Si_{0.09}N$ deposited on corundum sheets after 15-hour isothermal oxidation at 850 °C (a and d), 900 °C (b and e), and 950 °C (c and f).

Fig. 9 Cross-sectional SEM images (a, b, and c) and corresponding elemental maps (d, e, and f) of $Ti_{0.48}Al_{0.38}Si_{0.14}N$ deposited on corundum sheets after 15-hour isothermal oxidation at 850 °C (a and d), 900 °C (b and e), and 950 °C (c and f).

Fig. 10 Consumed nitride thickness on $Ti_{0.52}Al_{0.48}N$, $Ti_{0.53}Al_{0.38}Si_{0.09}N$, $Ti_{0.43}Al_{0.48}Si_{0.09}N$, and $Ti_{0.48}Al_{0.38}Si_{0.14}N$ coatings after 15-hour isothermal oxidation at 850, 900, and 950 °C.

Fig. 11 Cross-sectional SEM images (a, b, and c) and corresponding elemental maps (d, e, and f) of $Ti_{0.48}Al_{0.38}Si_{0.14}N$ after deposited on corundum sheets 10-hour isothermal oxidation at 850 °C (a and d), 900 °C (b and e), and 950 °C (c and f).

- Both thermal stability and oxidation resistance are enhanced after Si-alloying.
- The effect of Si on the oxidation behavior of Ti-Al-Si-N is multifold.
- The Si/Ti ratio of 0.21 retards the anatase-to-rutile transformation most.
- Si-alloying leads to an abnormal oxidation behavior of Ti-Al-N coatings.

Figure 1

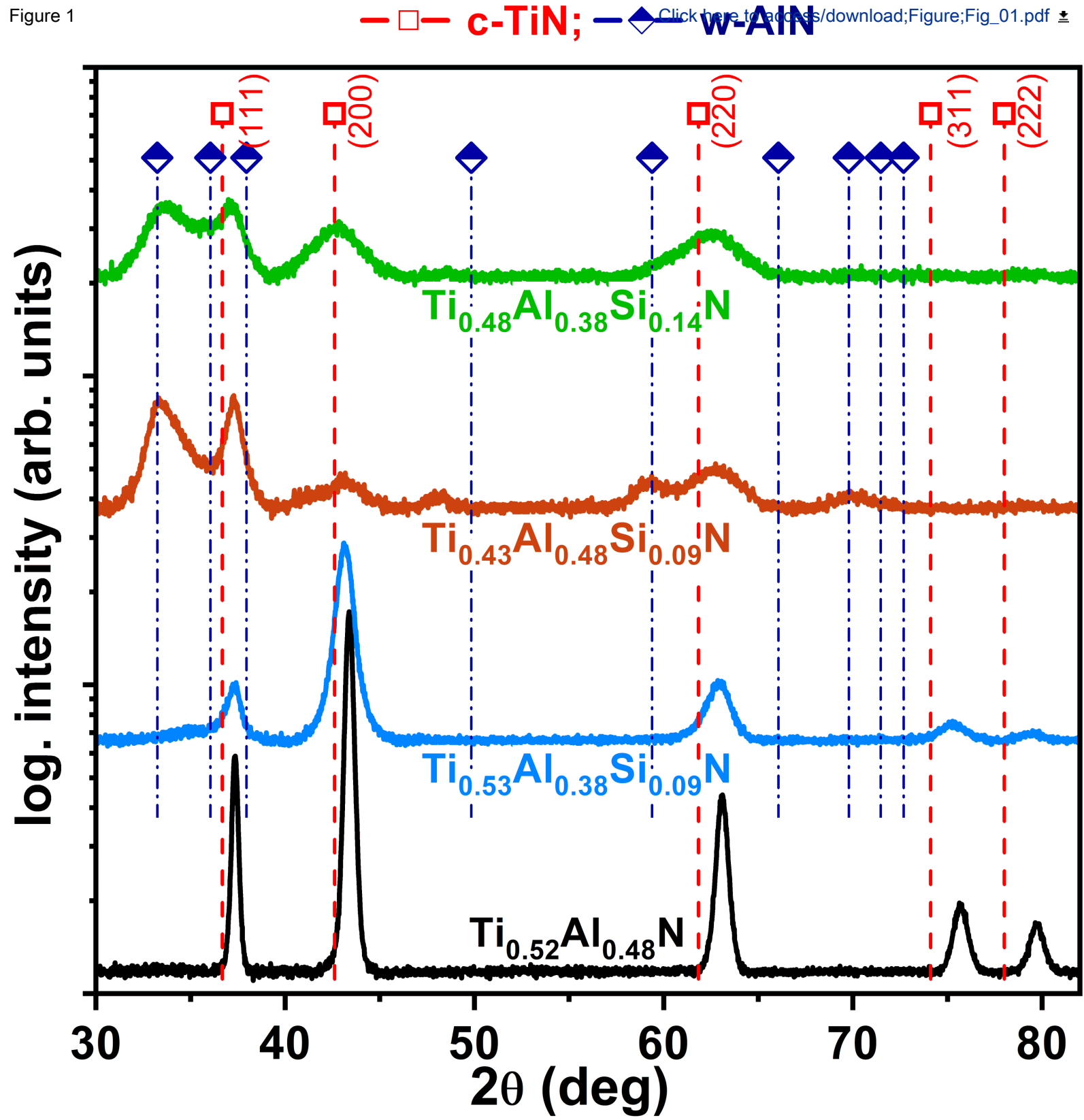
c-TiN;
w-AlN
(111)
(200)
(220)
(311)
(222)
Ti0.48Al0.38Si0.14N
Ti0.43Al0.48Si0.09N
Ti0.53Al0.38Si0.09N
Ti0.52Al0.48N
log. intensity (arb. units)
30
40
50
60
70
80
2θ (deg)

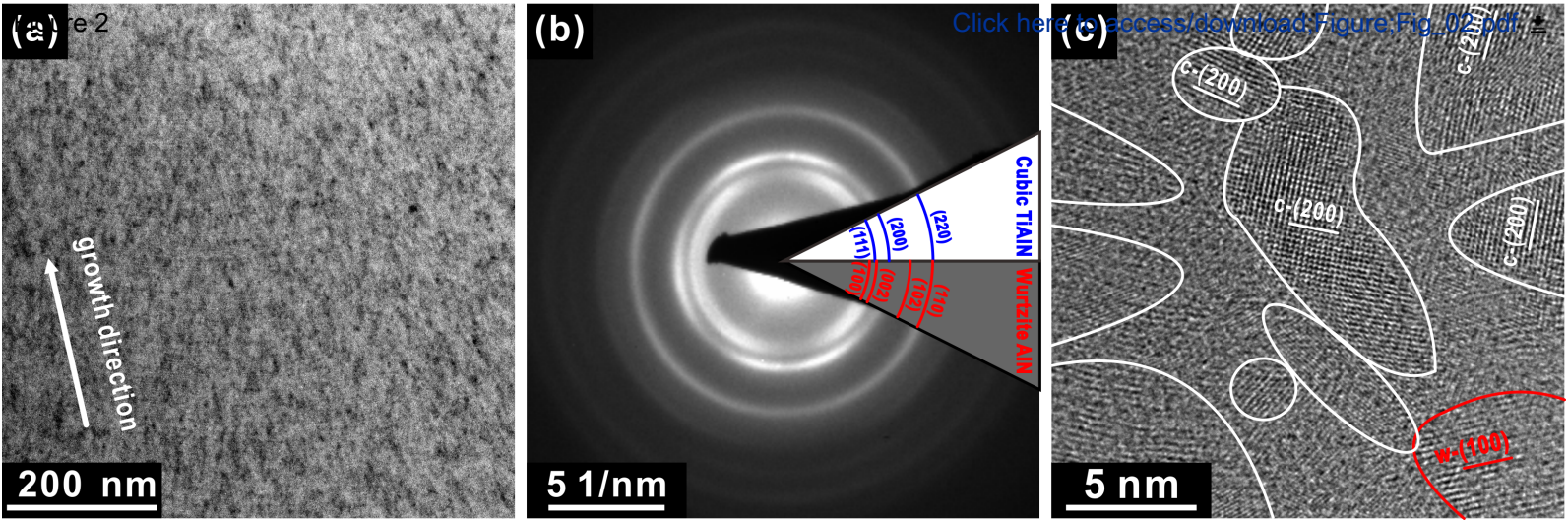

Figure 3

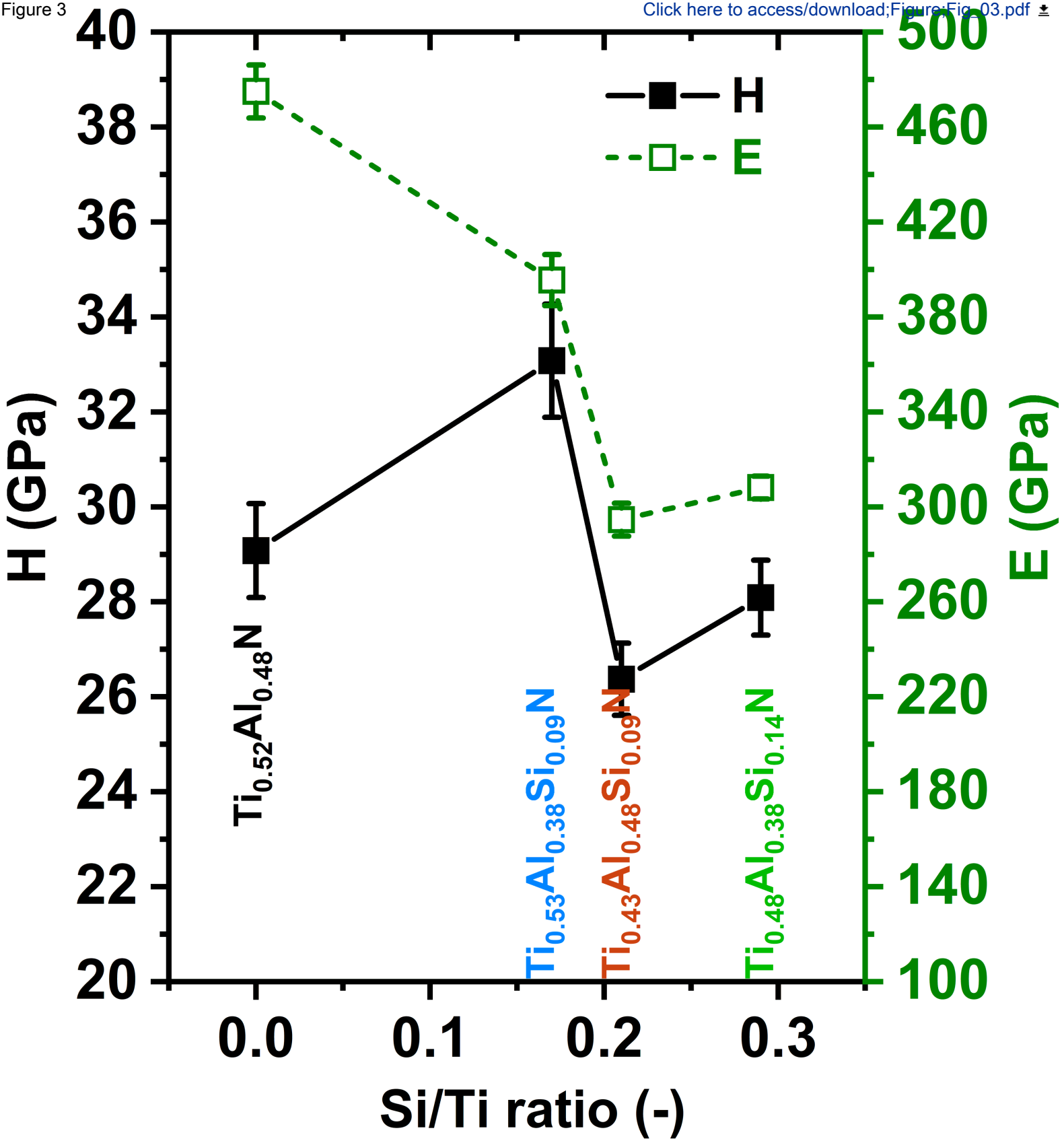

Figure 4

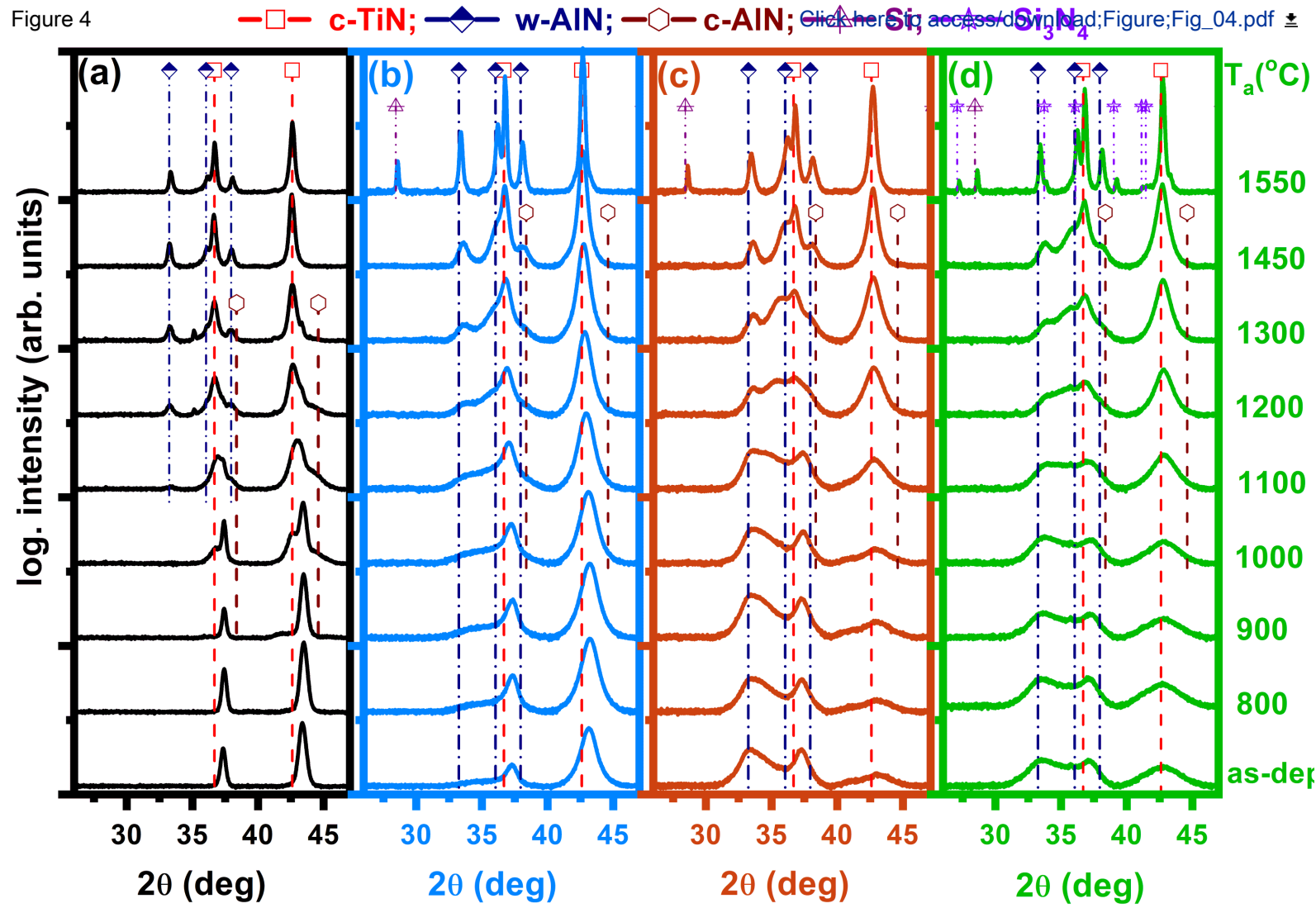
c-TiN;
w-AlN;
c-AlN;
Si;
Si_3N_4
(a)
(b)
(c)
(d)
T_a(°C)
1550
1450
1300
1200
1100
1000
900
800
as-dep
log. intensity (arb. units)
30
35
40
45
2θ (deg)

Figure 5

Click here to access/download;Figure;Fig_05.pdf

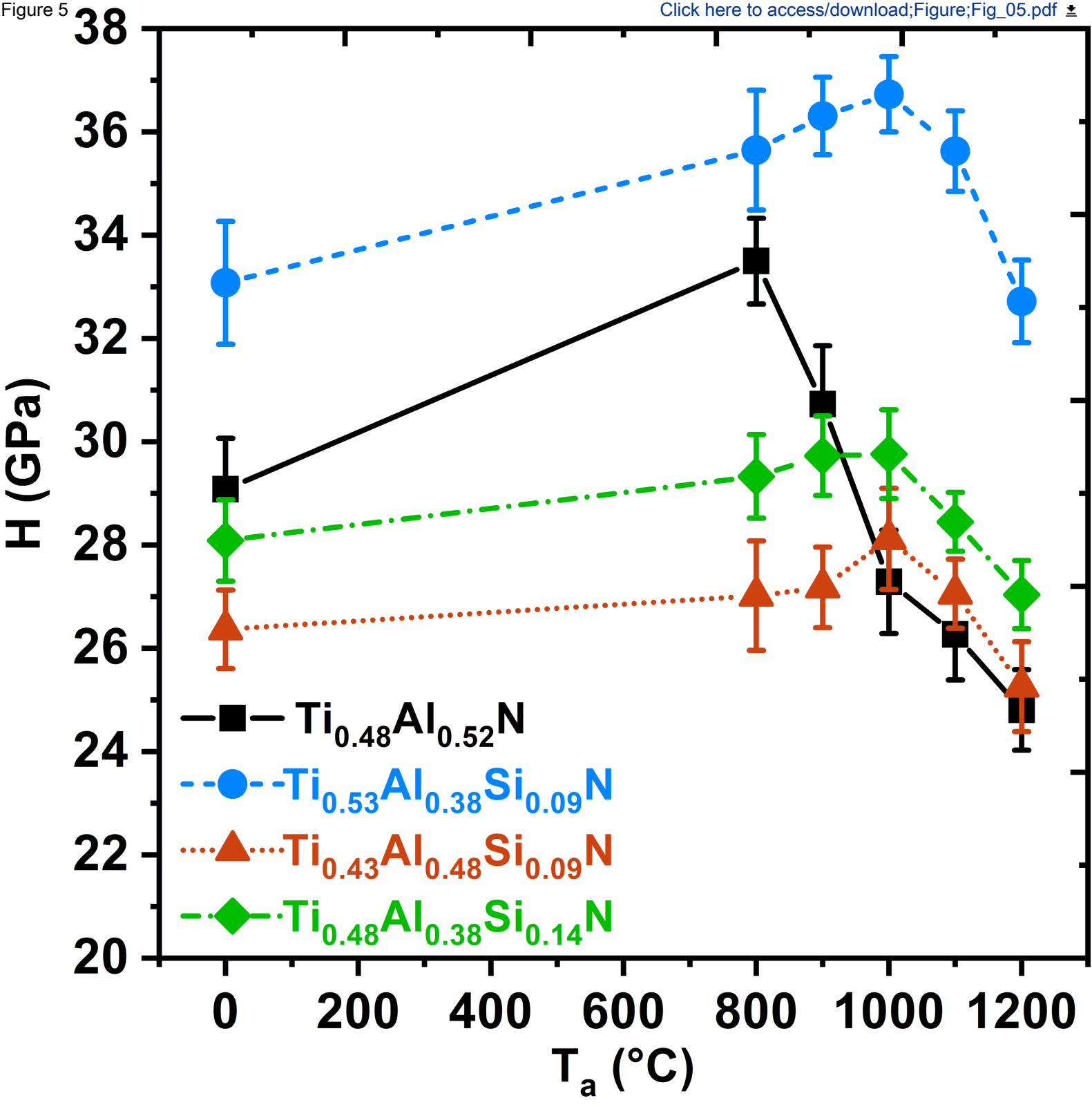

Figure 6

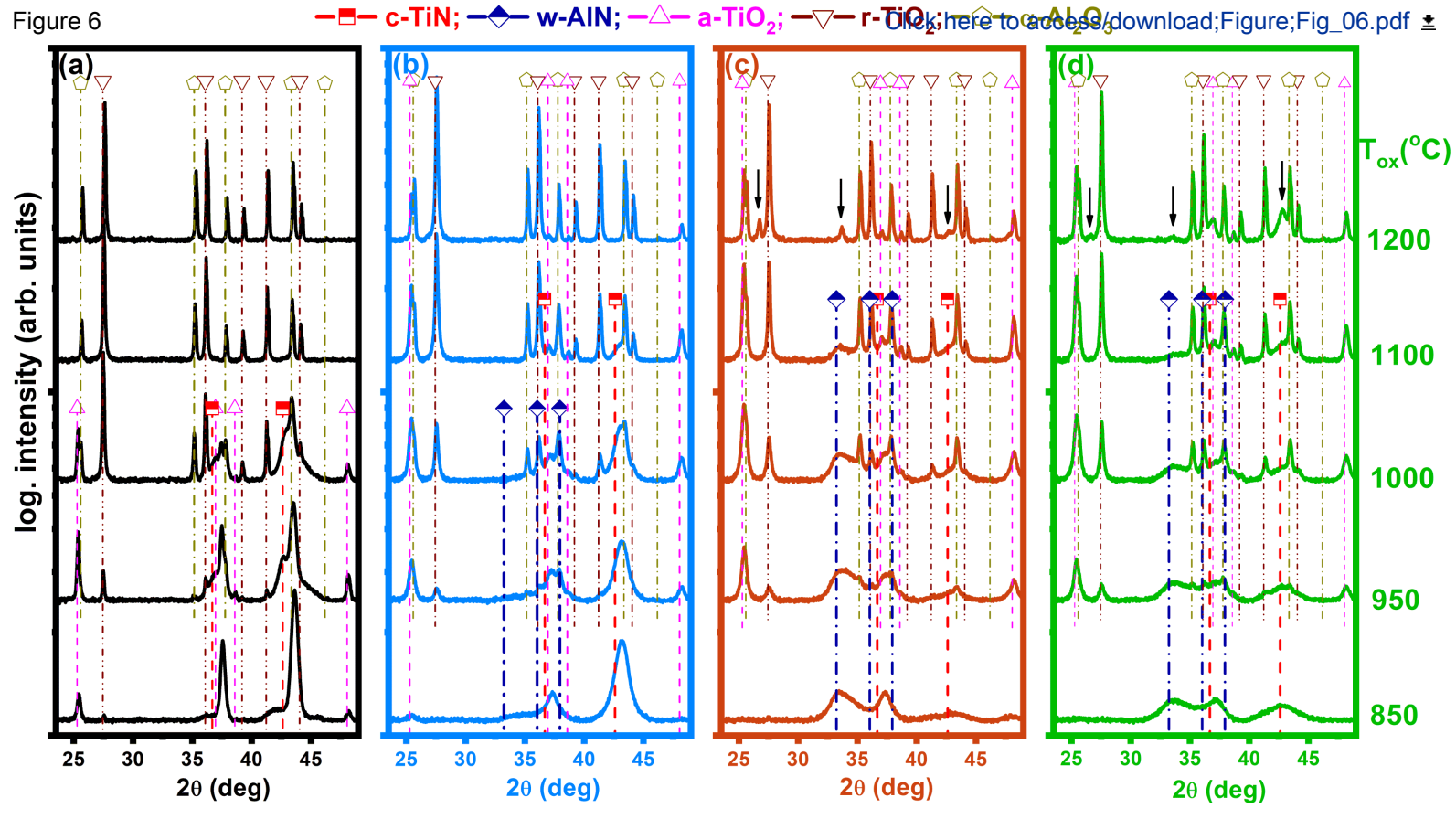
c-TiN; w-AlN; a-TiO2; r-TiO2; α-Al2O3
Click here to access/download;Figure;Fig_06.pdf
(a)
(b)
(c)
(d)
log. intensity (arb. units)
2θ (deg)
25 30 35 40 45
Tox(°C)
1200
1100
1000
950
850

Figure 7

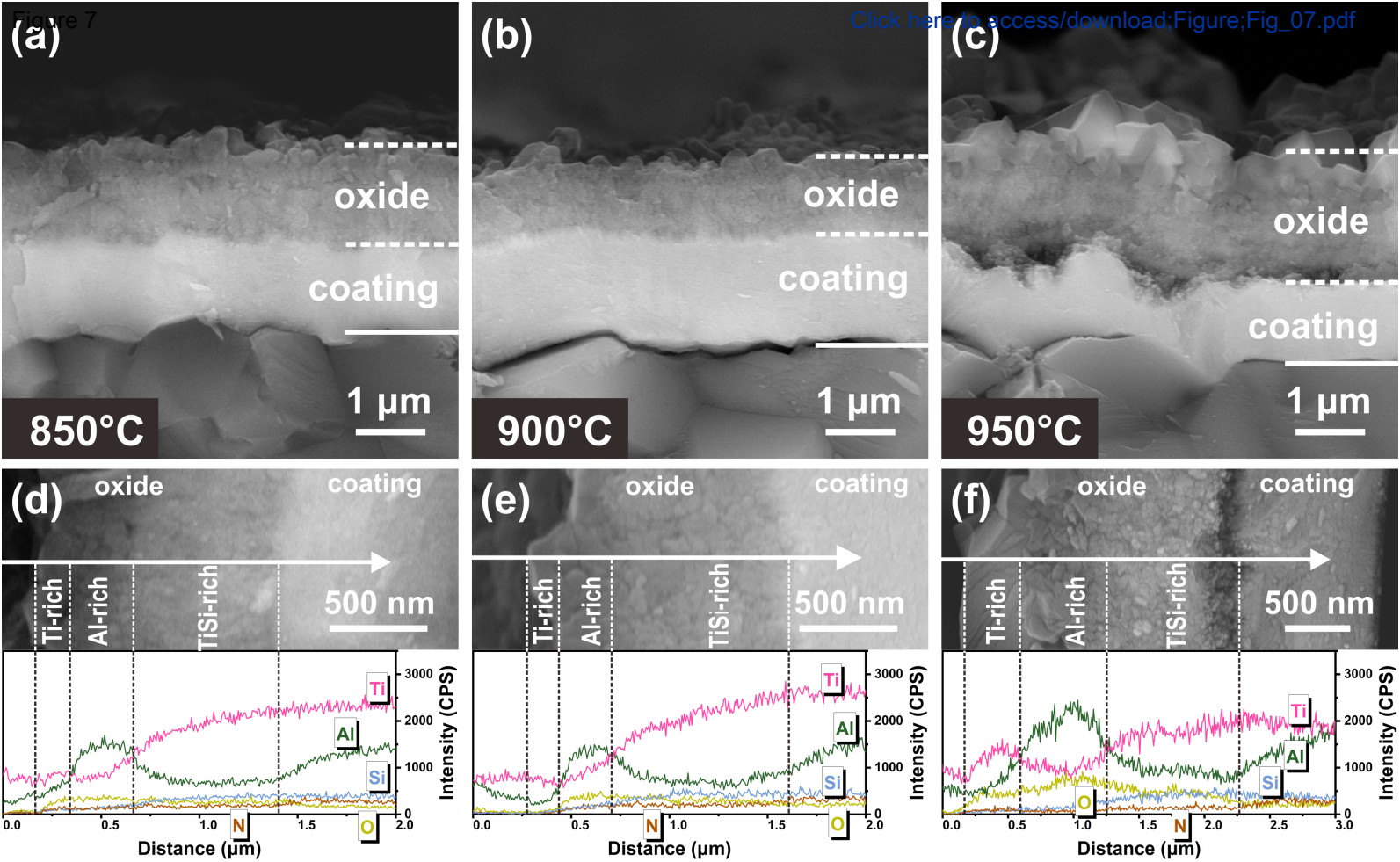

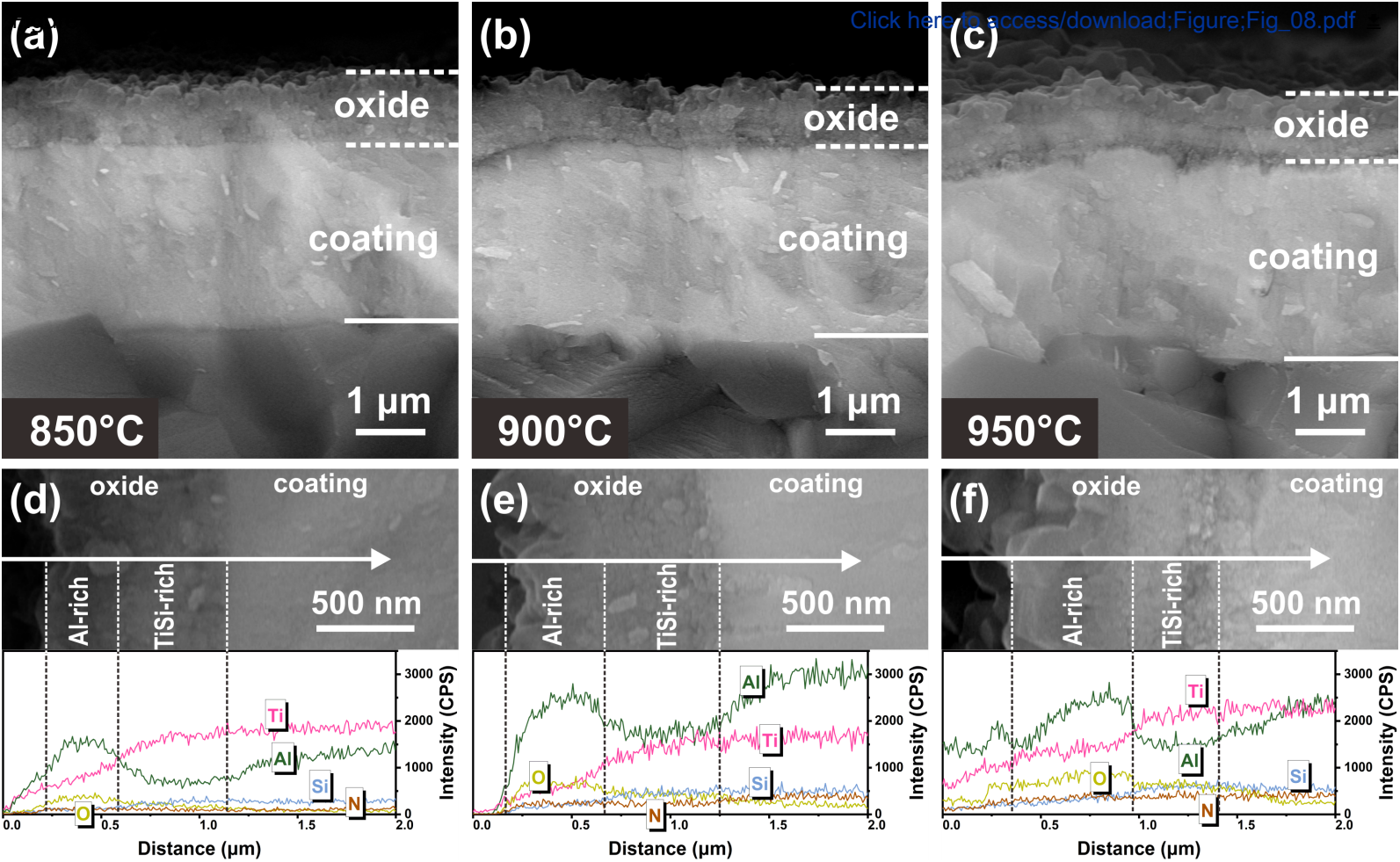

Figure 9

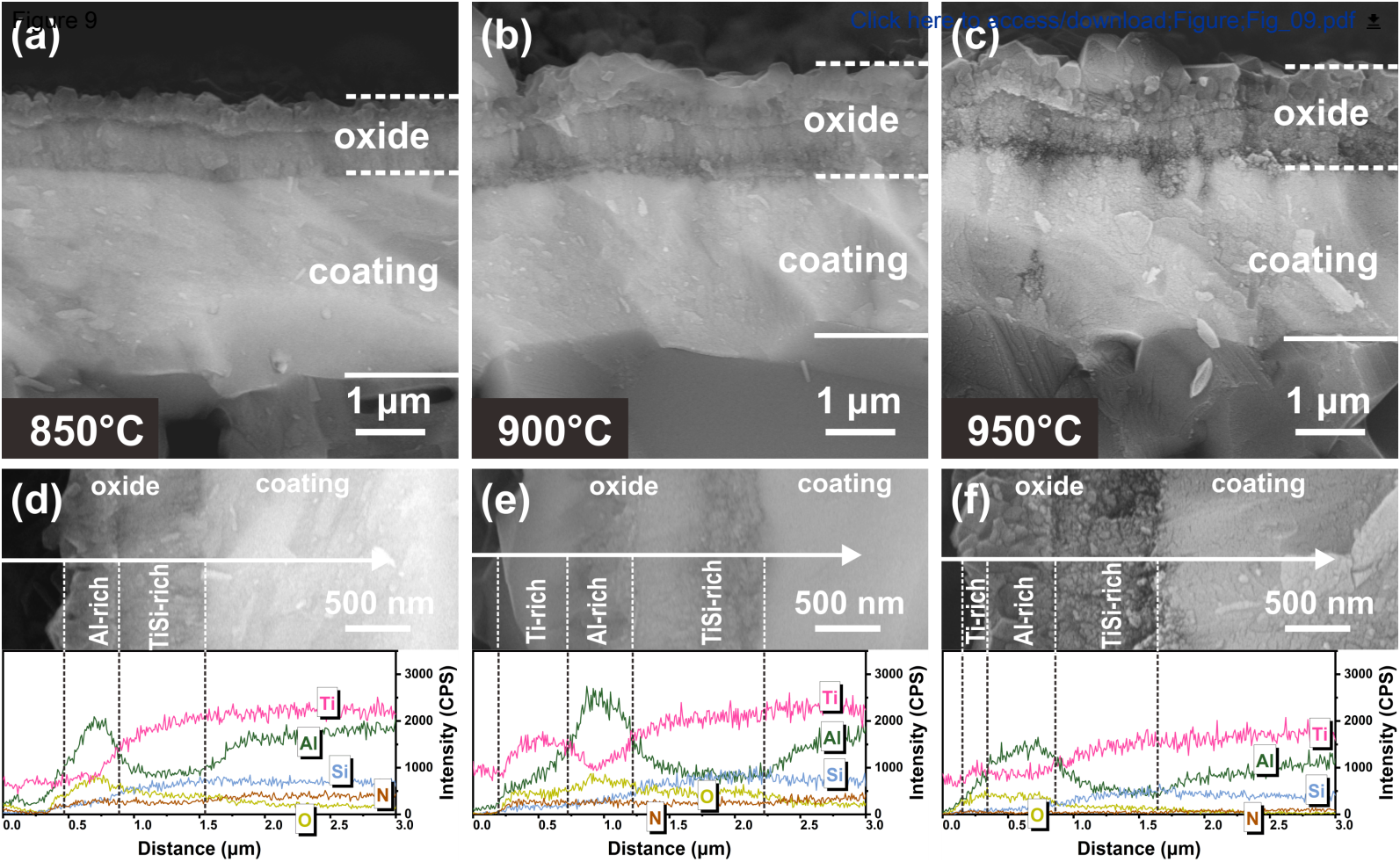

Figure 10

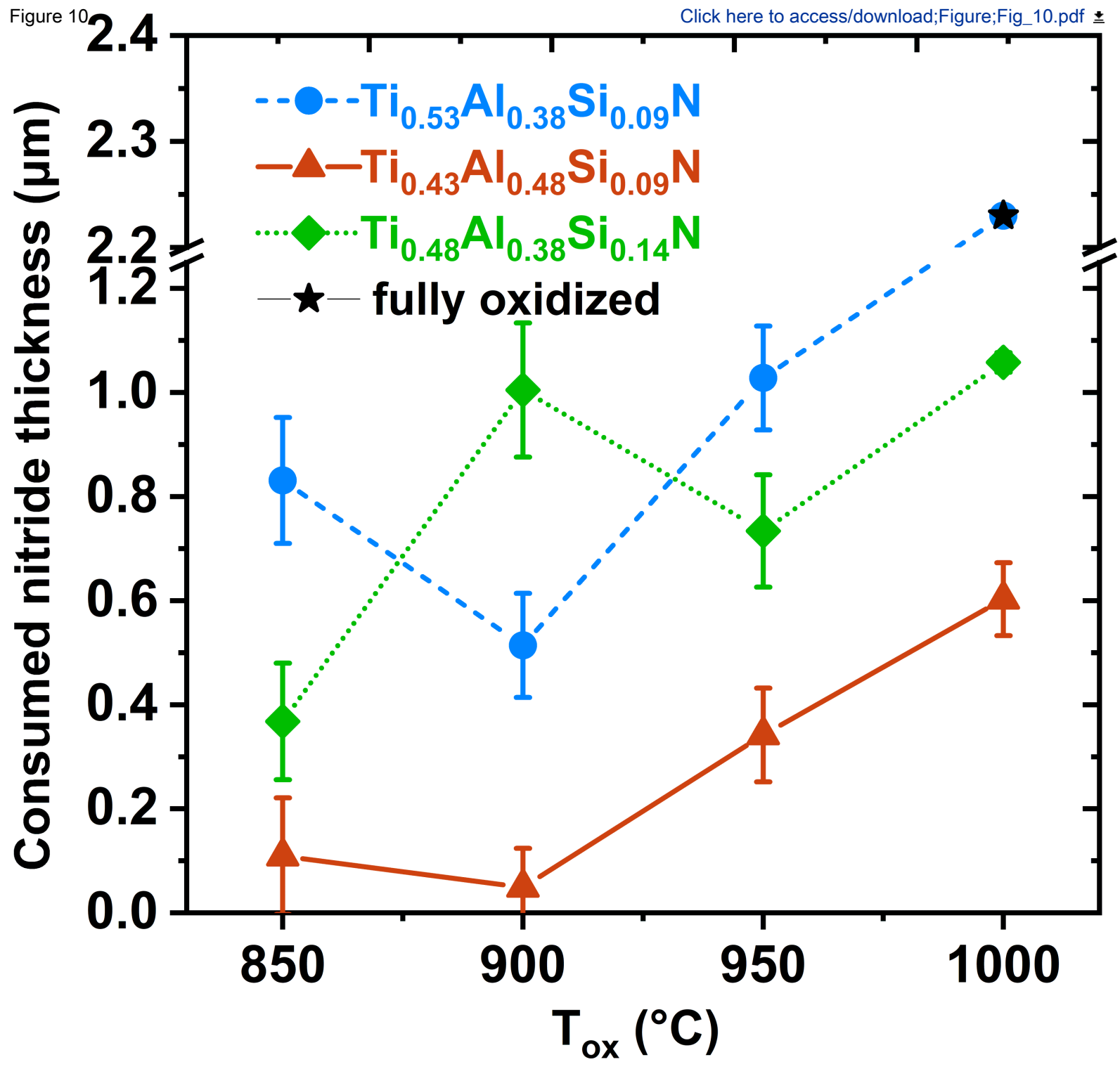

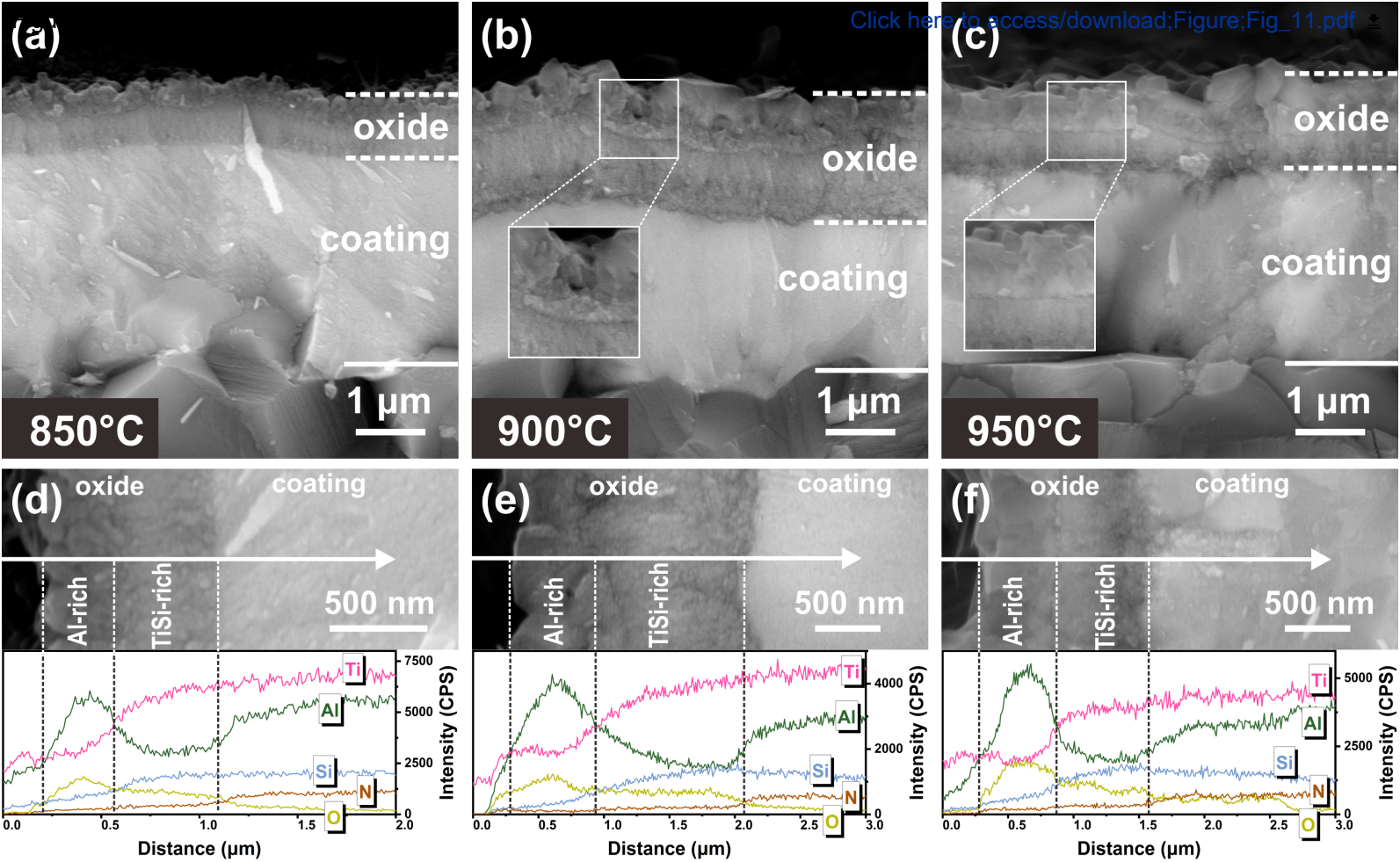

Credit Author Statement:

Zhe R. Liu: Visualization, Writing- Original draft preparation. **Fei Pei**: Investigation. **Li Chen**: Conceptualization, Methodology, Writing - Review & Editing, and Funding acquisition. **Paul H. Mayrhofer:** Writing - Review & Editing.